The Astrophysical Journal, 862:98 (9pp), 2018 August 1 https://doi.org/10.3847/1538-4357/aacc28

Neutron Star Equation of State from the Quark Level in Light of GW170817

Zhen-Yu Zhu[1], En-Ping Zhou[2], and Ang Li[1]
[1] Department of Astronomy, Xiamen University, Xiamen, Fujian 361005, People's Republic of China; liang@xmu.edu.cn
[2] State Key Laboratory of Nuclear Science and Technology and School of Physics, Peking University, Beijing 100871, People's Republic of China
Received 2018 February 26; revised 2018 June 8; accepted 2018 June 10; published 2018 July 26

Abstract

The matter state inside neutron stars (NSs) is an exciting problem in astrophysics, nuclear physics, and particle physics. The equation of state (EOS) of NSs plays a crucial role in the present multimessenger astronomy, especially after the event of GW170817. We propose a new NS EOS, "QMF18," from the quark level, which describes robust observational constraints from a free-space nucleon, nuclear matter saturation, heavy pulsar measurements, and the tidal deformability of the very recent GW170817 observation. For this purpose, we employ the quark mean-field model, which allows us to tune the density dependence of the symmetry energy and effectively study its correlations with the Love number and the tidal deformability. We provide tabulated data for the new EOS and compare it with other recent EOSs from various many-body frameworks.

Key words: dense matter – equation of state – gravitational waves – stars: neutron

1. Introduction

Neutron stars (NSs) are by far one of the most interesting observational objects, because their complexity remains mysterious. Multimessenger observations with advanced telescopes such as Advanced LIGO and VIRGO (e.g., Abbott et al. 2017), FAST (e.g., Li & Pan 2016), SKA (e.g., Watts et al. 2015), *NICER* (e.g., Özel et al. 2016), *HXMT* (e.g., Li et al. 2018b), eXTP (e.g., Watts et al. 2018), and AXTAR (e.g., Ray et al. 2010), will hopefully provide precise measurements of their mass and/or radius, thus improving our current knowledge of such stellar objects and their equations of states (EOSs), especially for the high-density inner crust with densities above the nuclear saturation density $\rho_0 \sim 0.16$ fm^{-3}. The dense matter EOS is also closely related to the scientific goals of all advanced radioactive beam facilities (e.g., Danielewicz et al. 2002; Tsang et al. 2009).

Nowadays, the EOS of symmetric nuclear matter (SNM; Danielewicz et al. 2002) ($\beta \equiv \frac{\rho_n - \rho_p}{\rho_n + \rho_p} = 0$) is relatively well-constrained, with ρ_n and ρ_p as the neutron and proton density, respectively. Matter with nonzero isospin asymmetry remains unknown, largely due to the uncertainty in the symmetry energy: $E_{\rm sym}(\rho) \approx [E(\rho, \beta) - E(\rho, 0)]/\beta^2$, with $E(\rho, \beta)$ being the energy per nucleon of nuclear matter at isospin asymmetry β and density ρ. Conflicts remain for the symmetry energy (especially its slope $L(\rho) = dE_{\rm sym}(\rho)/d\rho$) despite significant progress in constraining the symmetry energy around and below the nuclear matter saturation density (e.g., Tsang et al. 2009; Danielewicz & Lee 2014; Zhang & Chen 2015). At saturation density $\rho = \rho_0$, L may have a lower limit $\sim$20 MeV (Centelles et al. 2009) and an upper limit $>$170 MeV (Cozma et al. 2013). It characterizes the density dependence of the symmetry energy and largely dominates the ambiguity and stiffness of the EOS for dense nuclear matter and NS matter at the densities approached in NS cores, such as that for the cases of no strangeness phase transition (e.g., Li et al. 2006, 2007, 2010, 2015; Burgio et al. 2011; Hu et al. 2014b; Zhu et al. 2016). Therefore, it is a crucial parameter for NS EOS and related studies.

Recently, from the observation of GW170817, the LIGO +Virgo Collaborations placed a clean upper limit on the tidal deformability of the compact object, $\Lambda = (2/3)k_2/(GM/c^2R)^5$, with k_2 being the second Love number. Since the star radius is rather sensitive to the symmetry energy (essentially its slope L), with the maximum mass only slightly modified (e.g., Lattimer & Prakash 2004, 2001; Li & Steiner 2006), this Λ measurement might possibly put an independent constraint on L, as has been previously discussed in Fattoyev et al. (2013, 2018) and Zhang et al. (2018). Λ describes the size of the induced mass quadrupole moment when reacting to a certain external tidal field (Damour et al. 1992; Damour & Nagar 2009). If a low-spin prior is assumed for both stars in the binary, which is reasonable considering the magnetic braking during the binary evolution, the tidal deformability for a $1.4\,M_\odot$ star (denoted as $\Lambda(1.4)$ in below) was concluded to be smaller than 800 (a more loosely constrained upper limit of 1400 is found for the high-spin prior case) (Abbott et al. 2017). Based on the GW170817 observation, several recent studies have reported their constraints on NS EOS (e.g., Bauswein et al. 2017; Ma et al. 2017; Margalit & Metzger 2017; Ai et al. 2018; Annala et al. 2018, 2017; Drago & Pagliara 2018; Fattoyev et al. 2018; Krastev & Li 2018; Nandi & Char 2018; Paschalidis et al. 2018; Radice et al. 2018; Ruiz et al. 2018; Shibata et al. 2017; Zhang et al. 2018) and QS EOS (Zhou et al. 2018).

The objective of the present study is to make use of the new GW170817 constraint, combined with available terrestrial nuclear structure/reaction experiments (e.g., Danielewicz et al. 2002; Tsang et al. 2009; Li & Han 2013; Danielewicz & Lee 2014; Zhang & Chen 2015) and astrophysical observations (Demorest et al. 2010; Antoniadis et al. 2013; Fonseca et al. 2016), for the determination of nuclear saturation properties, and to construct a new NS EOS from the quark level. The employed EOS model enables us to fine-tune the L value and consistently study the Λ versus L dependence, with well-reproduced robust observables from laboratory nucleons, nuclear saturation, heavy-ion collisions (HIC), and heavy pulsars.

The paper is organized as follows. In Section 2, we describe the theoretical framework to consistently describe a nucleon and many-body nucleonic system from a quark potential, including the necessary fitting of the quark potential parameters and the meson coupling parameters from a vacuum nucleon

and empirical nuclear saturation properties, respectively. In Section 3, the NS EOSs and the corresponding mass–radius relations, as well as the tidal deformabilities, are discussed, and are compared with the mass measurements of heavy pulsars (Demorest et al. 2010; Antoniadis et al. 2013; Fonseca et al. 2016) and the tidal deformability of GW170817 (either $\Lambda(1.4)$ or $\tilde{\Lambda}$) (Abbott et al. 2017). The tabulated EOS of the new "QMF18" model is also provided and comparisons are made with other recent EOSs from various many-body theories. A summary and future perspectives are presented in Section 4.

2. Model

To carry out a study of a nuclear many-body system from the quark level, one first constructs a nucleon from confined quarks, by a finite confining region (characterized by a constant energy per unit volume, the bag constant B; Chodos et al. 1974) or by constituent quarks with a harmonic oscillator confining potential (Barik & Dash 1986; Frederico et al. 1989). Then, nucleons interact with point-like mesons. Since the meson fields modify the internal quark motion, the mesons couple not to point-like nucleons but self-consistently to confined quarks. The effects of the nucleon velocity, as well as the effect of antisymmetrization, are usually neglected, and the calculation is done in the mean-field approximation. The first model is often called the quark-meson coupling (QMC; e.g., Guichon 1988; Saito et al. 2007; Barik et al. 2013; Mishra et al. 2015, 2016) and the next model is called the quark mean-field (QMF) model (e.g., Toki et al. 1998; Shen & Toki 2000, 2002; Hu et al. 2014a, 2014b; Xing et al. 2016; Zhu & Li 2018). The QMC and QMF models may be viewed as a variation of the relativistic mean-field (RMF) model (e.g., Walecka 1974; Boguta & Bodmer 1977; Serot & Walecka 1986; Müller & Serot 1996; Horowitz & Piekarewicz 2001), which is from the hadron level. The RMF model, including its extension of the isoscalar Fock terms (e.g., Sun et al. 2008; Long et al. 2012; Zhu et al. 2016; Li et al. 2018a), has been widely used for NS studies.

In this work, following the methodology of the QMC and QMF models, we start with a flavor-independent potential $U(r)$ that confines the constituent quarks inside a nucleon. Details can be found in Barik et al. (2013), Mishra et al. (2015, 2016), Xing et al. (2016), and Zhu & Li (2018). Here for completeness, we only write necessary formulas. The confining potential is written as (Barik & Dash 1986)

$$U(r) = \frac{1}{2}(1+\gamma^0)(ar^2 + V_0), \tag{1}$$

with the parameters a and V_0 to be determined from the vacuum nucleon properties. The Dirac equation of the confined quarks is written as

$$[\gamma^0(\epsilon_q - g_{\omega q}\omega - \tau_{3q}g_{\rho q}\rho) - \boldsymbol{\gamma}\cdot\boldsymbol{p} - (m_q - g_{\sigma q}\sigma) - U(r)]\psi_q(\boldsymbol{r}) = 0. \tag{2}$$

Hereafter, $\psi_q(\boldsymbol{r})$ is the quark field, and σ, ω, and ρ are the classical meson fields. $g_{\sigma q}$, $g_{\omega q}$, and $g_{\rho q}$ are the coupling constants of σ, ω, and ρ mesons with quarks, respectively. τ_{3q} is the third component of isospin matrix. This equation can be solved exactly and its ground-state solution for energy is

$$(\epsilon'_q - m'_q)\sqrt{\frac{\lambda_q}{a}} = 3, \tag{3}$$

where $\lambda_q = \epsilon^*_q + m^*_q$, $\epsilon'_q = \epsilon^*_q - V_0/2$, $m'_q = m^*_q + V_0/2$. The effective single quark energy is given by $\epsilon^*_q = \epsilon_q - g_{q\omega}\omega - \tau_{3q}g_{q\rho}\rho$ and the effective quark mass is given by $m^*_q = m_q - g_{\sigma q}\sigma$, with the quark mass $m_q = 300$ MeV.

The zeroth-order energy of the nucleon core $E^0_N = \sum_q \epsilon^*_q$ can be obtained by solving Equation (3). The contributions of the center-of-mass correction $\epsilon_{c.m.}$, pionic correction δM^π_N, and gluonic correction $(\Delta E_N)_g$ are also taken into account, as done in Barik & Dash (1986), Barik et al. (2013), Mishra et al. (2015, 2016), Xing et al. (2016), and Zhu & Li (2018). With these corrections to the energy, we can then determine the mass of a nucleon in medium:

$$M^*_N = E^0_N - \epsilon_{c.m.} + \delta M^\pi_N + (\Delta E_N)_g. \tag{4}$$

The nucleon radius is written as

$$\langle r^2_N\rangle = \frac{11\epsilon'_q + m'_q}{(3\epsilon'_q + m'_q)(\epsilon'^2_q - m'^2_q)}. \tag{5}$$

From reproducing the nucleon mass and radius (M_N, r_N) in free space, we determine the potential parameters (a and V_0) in Equation (1). $V_0 = -62.257187$ MeV and $a = 0.534296$ fm^{-3} are obtained by fitting $M_N = 939$ MeV and $r_N = 0.87$ fm.

We then move from a single nucleon to a nucleonic many-body system for the study of infinite nuclear matter and NSs. Nuclear matter is described by point-like nucleons and mesons interacting through exchange of σ, ω, ρ mesons. The Lagrangian is written as (see also, for example, Li et al. 2008)

$$\begin{aligned}\mathcal{L} = {} & \overline{\psi}(i\gamma_\mu\partial^\mu - M^*_N - g_{\omega N}\omega\gamma^0 - g_{\rho N}\rho\tau_3\gamma^0)\psi \\ & - \frac{1}{2}(\nabla\sigma)^2 - \frac{1}{2}m^2_\sigma\sigma^2 - \frac{1}{3}g_2\sigma^3 - \frac{1}{4}g_3\sigma^4 \\ & + \frac{1}{2}(\nabla\rho)^2 + \frac{1}{2}m^2_\rho\rho^2 + \frac{1}{2}(\nabla\omega)^2 \\ & + \frac{1}{2}m^2_\omega\omega^2 + \frac{1}{2}g^2_{\rho N}\rho^2\Lambda_v g^2_{\omega N}\omega^2,\end{aligned} \tag{6}$$

where $g_{\omega N}$ and $g_{\rho N}$ are the nucleon coupling constants for ω and ρ mesons. From the quark counting rule, we obtain $g_{\omega N} = 3g_{\omega q}$ and $g_{\rho N} = g_{\rho q}$. The calculation of confined quarks gives the relation of effective nucleon mass M^*_N as a function of σ field,

Table 1
Saturation Properties Used in This Study for the Fitting of New Sets of Meson Coupling Parameters

ρ_0 (fm^{-3})	E/A (MeV)	K (MeV)	$E_{\rm sym}$ (MeV)	L (MeV)	M^*_N/M_N /
0.16	−16	240	31	20/40/60/80	0.77

Note. The table lists the saturation density ρ_0 (in fm^{-3}) and the corresponding values at the saturation point for the binding energy E/A (in MeV), the incompressibility K (in MeV), the symmetry energy $E_{\rm sym}$ (in MeV), the symmetry energy slope L (in MeV), and the ratio between the effective mass and free nucleon mass M^*_N/M_N.

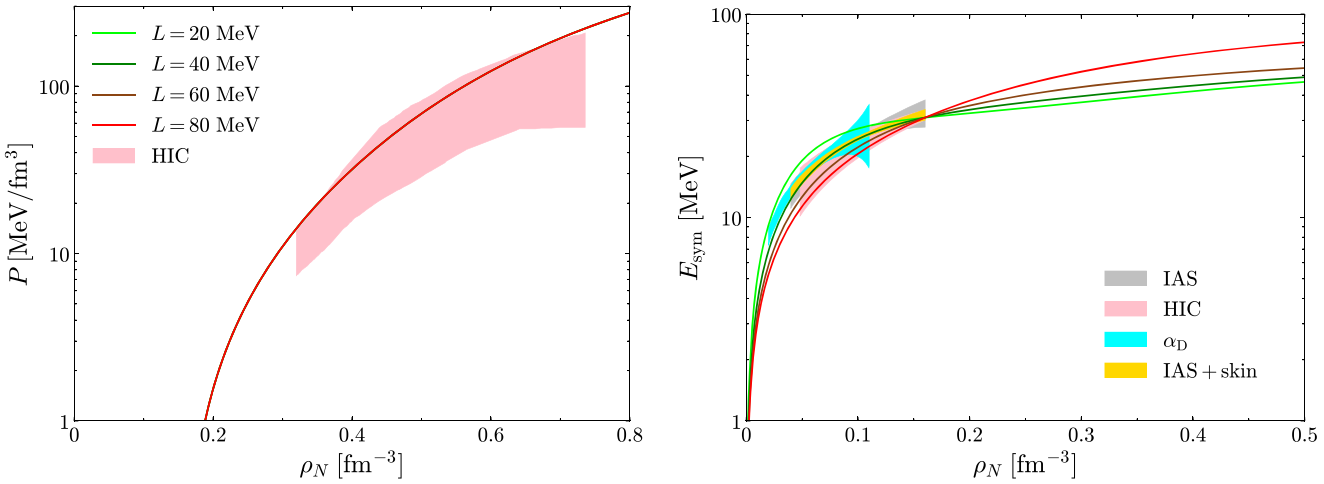

Figure 1. (Left panel) Pressure as a function of nucleon number density for SNM, together with the constraint from collective flow in HIC (Danielewicz et al. 2002; note here that the results from different parameter sets with different values of symmetry energy slope L are the same in SNM). (Right panel) Symmetry energy as a function of nucleon number density, with four different values of symmetry energy slope L. Colorful shadow regions represent the constraints from isobaric analog states (IAS), from transport in HIC (Tsang et al. 2009), from electric dipole polarizability in ^{208}Pb (α_D) (Zhang & Chen 2015), and from IAS and neutron skins (IAS+skin) (Danielewicz & Lee 2014), respectively.

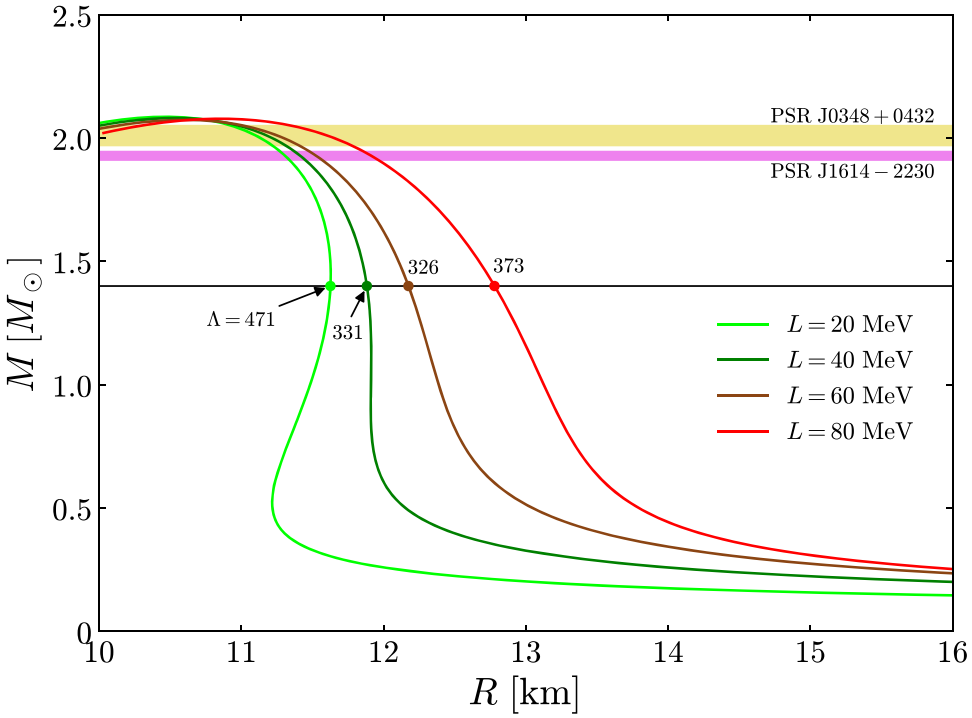

Figure 2. Mass–radius curves for four EOSs with different values of L (20, 40, 60, 80 MeV), together with the mass measurements for two recent massive stars: PSR J1614-2230 (Demorest et al. 2010; Fonseca et al. 2016) and PSR J0348+0432 (Antoniadis et al. 2013). The horizontal black line indicates $M = 1.4\ M_\odot$. The numbers mark the Λ values for $1.4\ M_\odot$ stars corresponding to colorful dots.

Table 2
Newly Fitted Meson Coupling Parameters from Using Table 1 as Input

L (MeV)	$g_{\sigma q}$	$g_{\omega q}$	$g_{\rho q}$	g_2 (fm^{-1})	g_3	Λ_v
20	3.8620366	2.9174838	6.9588083	14.6179599	−66.3442468	1.1080665
40	3.8620366	2.9174838	5.4129448	14.6179599	−66.3442468	0.7693664
60	3.8620366	2.9174838	4.5830609	14.6179599	−66.3442468	0.4306662
80	3.8620366	2.9174838	4.0459574	14.6179599	−66.3442468	0.0919661

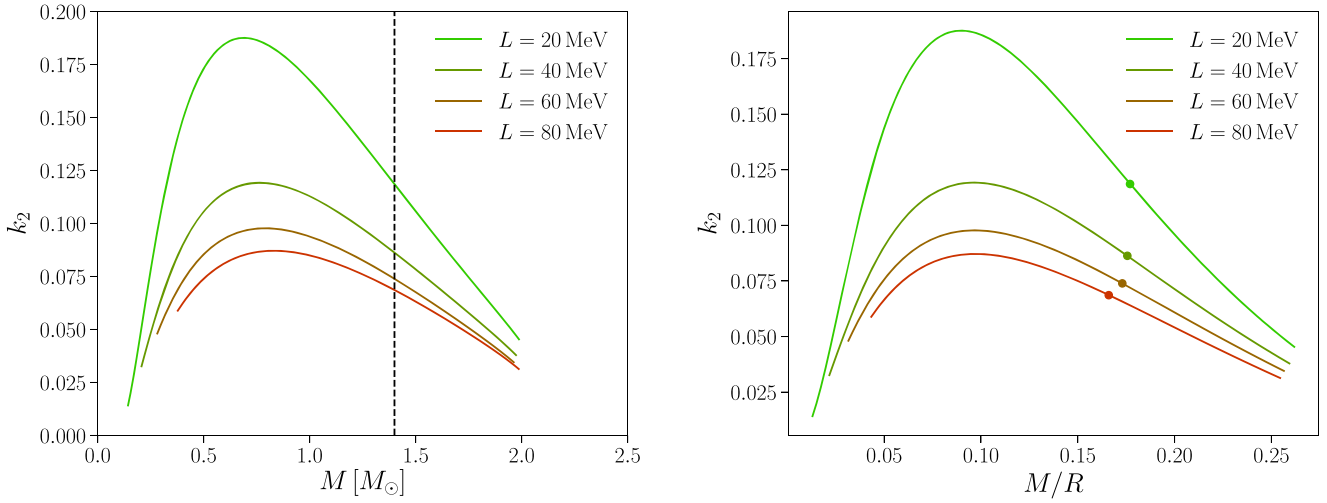

Figure 3. Love numbers as a function of the mass (left panel) and the compactness (right panel), for four EOSs with different values of L (20, 40, 60, 80 MeV). The vertical line and colorful dots indicate $M = 1.4\,M_\odot$.

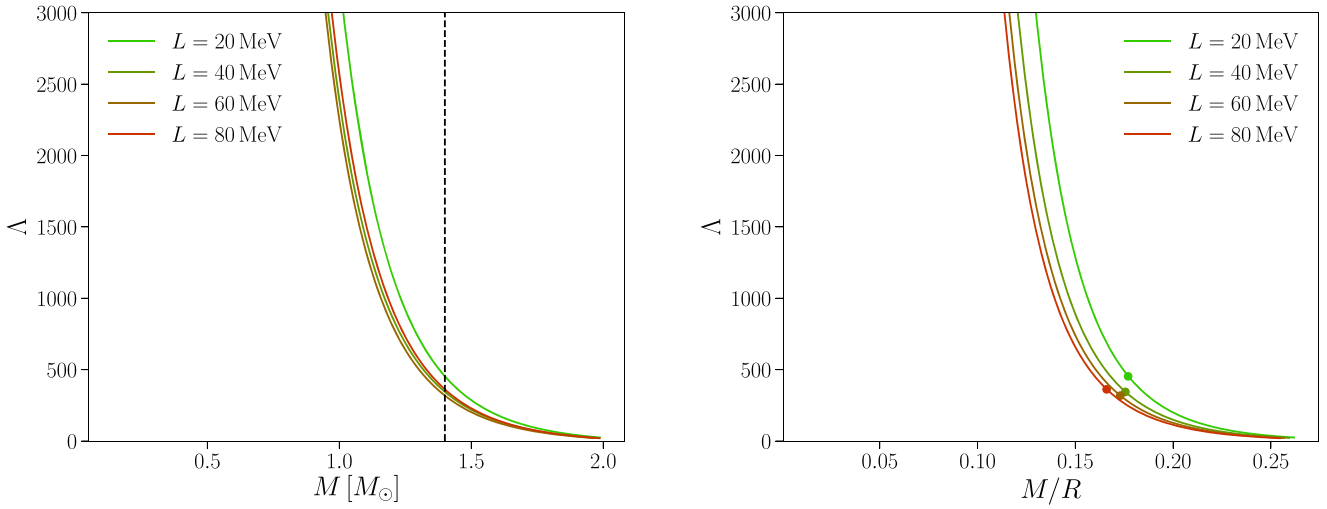

Figure 4. Same with Figure 3, but for the tidal deformabilities.

which defines the σ coupling with nucleons (depending on the parameter $g_{\sigma q}$). $m_\sigma = 510$ MeV, $m_\omega = 783$ MeV, and $m_\rho = 770$ MeV are the meson masses.

The equations of motion for mesons can be obtained by variation of the Lagrangian:

$$(i\gamma^\mu\partial_\mu - M_N^* - g_\omega\omega\gamma^0 - g_\rho\rho\tau_3\gamma^0)\psi = 0, \tag{7}$$

$$m_\sigma^2\sigma + g_2\sigma^2 + g_3\sigma^3 = -\frac{\partial M_N^*}{\partial\sigma}\langle\bar{\psi}\psi\rangle, \tag{8}$$

$$m_\omega^2\omega + \Lambda_v g_{\omega N}^2 g_{\rho N}^2\omega\rho^2 = g_{\omega N}\langle\bar{\psi}\gamma^0\psi\rangle, \tag{9}$$

$$m_\rho^2\rho + \Lambda_v g_{\rho N}^2 g_{\omega N}^2\rho\omega^2 = g_{\rho N}\langle\bar{\psi}\tau_3\gamma^0\psi\rangle. \tag{10}$$

From these Lagrangian and equations of motion of nucleons and mesons, the energy density and pressure can be generated by the energy–momentum tensor:

$$\begin{aligned}\mathcal{E} = &\frac{1}{\pi^2}\sum_{i=n,p}\int_0^{k_F^i}\sqrt{k^2 + M_N^{*2}}\,k^2dk \\ &+ \frac{1}{2}m_\sigma^2\sigma^2 + \frac{1}{3}g_2\sigma^3 + \frac{1}{4}g_3\sigma^4 \\ &+ \frac{1}{2}m_\omega^2\omega^2 + \frac{1}{2}m_\rho^2\rho^2 \\ &+ \frac{3}{2}\Lambda_v g_{\rho N}^2 g_{\omega N}^2\rho^2\omega^2,\end{aligned} \tag{11}$$

$$\begin{aligned}P = &\frac{1}{3\pi^2}\sum_{i=n,p}\int_0^{k_F^i}\frac{k^4}{\sqrt{k^2 + M_N^{*2}}}dk \\ &- \frac{1}{2}m_\sigma^2\sigma^2 - \frac{1}{3}g_2\sigma^3 - \frac{1}{4}g_3\sigma^4 \\ &+ \frac{1}{2}m_\omega^2\omega^2 + \frac{1}{2}m_\rho^2\rho^2 \\ &+ \frac{1}{2}\Lambda_v g_{\rho N}^2 g_{\omega N}^2\rho^2\omega^2.\end{aligned} \tag{12}$$

k_F^p (k_F^n) is the Fermi momentum for protons (neutron).

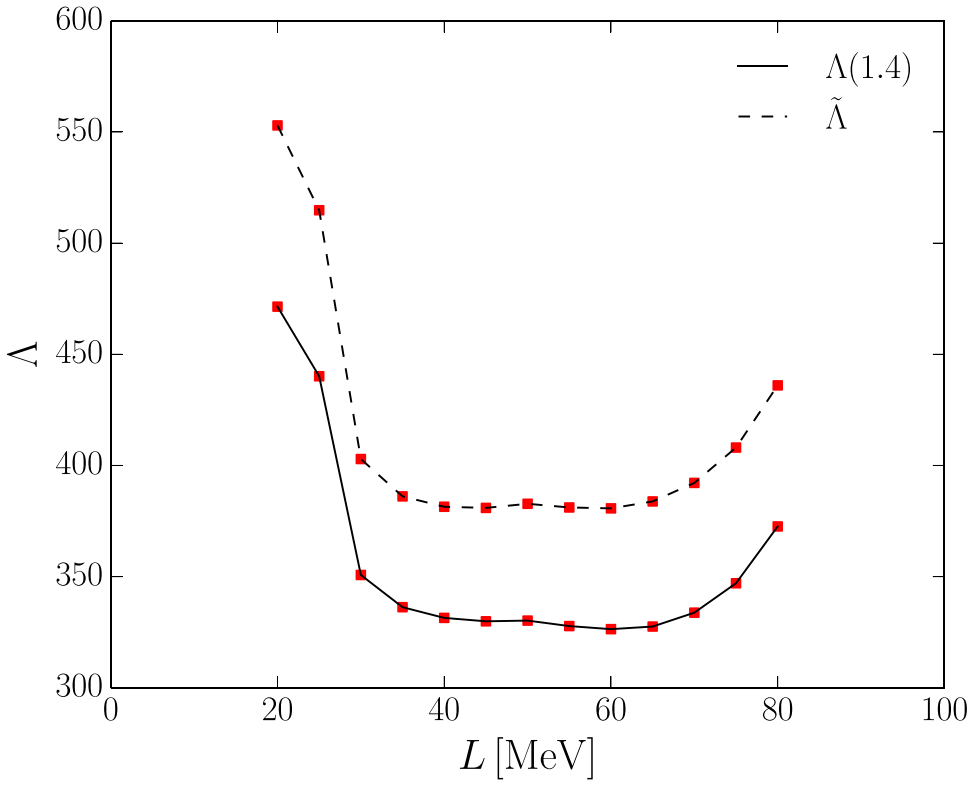

Figure 5. L dependence of tidal deformability: the tidal deformability for a 1.4 $M_\odot$ star (solid line) and the mass-weighed tidal deformability $\tilde{\Lambda}$ of a binary system with a chirp mass of 1.188 $M_\odot$, and mass ratio of 0.7 (dashed lined; Abbott et al. 2017).

There are six parameters ($g_{\sigma q}$, $g_{\omega q}$, $g_{\rho q}$, g_2, g_3, Λ_v) in the Lagrangian of Equation (6) and they will be determined by fitting the saturation density ρ_0 and the corresponding values at saturation point for the binding energy E/A, the incompressibility K, the symmetry energy $E_{\rm sym}$, the symmetry energy slope L, and the effective mass M_N^*. Those employed values are collected in Table 1. We use the intermediate value of incompressibility $K \approx 240 \pm 20$ MeV from Shlomo et al. (2006), Piekarewicz (2010). We also employ the most preferred values for ($E_{\rm sym}$, L) newly suggested by Li & Han (2013), namely $E_{\rm sym} = 31.6 \pm 2.66$ MeV, $L \approx 58.9 \pm 16$ MeV. Since the L value can be as low as ~20 MeV (Centelles et al. 2009), we choose four values of L (20, 40, 60, 80 MeV) as input for the parameter fitting according to our model capability, with the aim of studying its effect on the tidal deformability of binary NS system (Abbott et al. 2017). The model parameters obtained are collected in Table 2. Note that in our previous work (Zhu & Li 2018), with similar proper saturation properties (ρ_0, E/A, K, $E_{\rm sym}$, L, M_N^*) from terrestrial dense-matter measurements, the high-density EOS failed to pass the two-solar-mass constraint from massive pulsars (only around 1.6 times the solar mass). For the present purpose of introducing a new EOS for astrophysical studies, we refit the parameters by omitting the nonlinear terms of the ω meson field and successfully obtain a maximum mass fulfilling the two-solar-mass constraint for the first time within QMF.

3. EOS, Mass–Radius Relation, and Tidal Deformability

After the meson coupling parameters are established, the pressure and symmetry energy as functions of density for nuclear matter can be calculated. The results are shown in Figure 1, together with experimental regions (Danielewicz et al. 2002; Tsang et al. 2009; Danielewicz & Lee 2014; Zhang & Chen 2015). In the left panel, one can see that the SNM EOS is compatible with the flow constraint (Danielewicz et al. 2002). In the right panel, for different L the behaviors of symmetry energy versus density are all consistent with various nuclear experiments. Among them, the $L = 40$ MeV case lies comfortably inside all experimental boundaries.

We can move forward to calculate the EOS of NS matter, $P(\mathcal{E})$, by introducing the β-equilibrium and charge neutrality condition between nucleons and leptons:

$$\mu_n = \mu_e + \mu_p, \quad \rho_e + \rho_\mu = \mu_p, \tag{13}$$

where (μ_n, μ_e, μ_p)/(ρ_n, ρ_e, ρ_p) are the chemical potential/number density of neutrons, electrons, and protons, respectively. To describe the structure of the crust, we employ the quantal calculations of Negele & Vautherin (1973) for the medium-density regime ($0.001\ {\rm fm}^{-3} < \rho_N < 0.08\ {\rm fm}^{-3}$), and follow the formalism developed in Baym et al. (1971) for the outer crust ($\rho_N < 0.001\ {\rm fm}^{-3}$). The tidal Love number k_2 is obtained from the ratio of the induced quadrupole moment Q_{ij} to the applied tidal field E_{ij} (Damour et al. 1992; Hinderer 2008; Damour & Nagar 2009): $Q_{ij} = -k_2 \frac{2R^5}{3G} E_{ij}$, where R is the NS radius. The dimensionless tidal deformability Λ is related to the compactness M/R and the Love number k_2 through $\Lambda = \frac{2}{3} k_2 (M/R)^{-5}$.

The resulting mass–radius relations with $L = 20$, 40, 60, 80 MeV are presented in Figure 2. They all fulfill the recent observational constraints of the two massive pulsars of which the masses are precisely measured (Demorest et al. 2010; Antoniadis et al. 2013; Fonseca et al. 2016). Since these four EOSs have the same incompressibility ($K = 240$ MeV) and

Table 3
NS EOS for the QMF18 Model Newly Introduced in This Work

ϵ (g cm^{-3})	P (erg cm^{-3})	ρ_N (fm^{-3})
0.13855E+15	0.79586E+33	0.082
0.14365E+15	0.85234E+33	0.085
0.15216E+15	0.95144E+33	0.090
0.16920E+15	0.11706E+34	0.100
0.18626E+15	0.14226E+34	0.110
0.20336E+15	0.17145E+34	0.120
0.22047E+15	0.20433E+34	0.130
0.27203E+15	0.33950E+34	0.160
0.32393E+15	0.55426E+34	0.190
0.37631E+15	0.87679E+34	0.220
0.42926E+15	0.13315E+35	0.250
0.48293E+15	0.19385E+35	0.280
0.53741E+15	0.27149E+35	0.310
0.59282E+15	0.36752E+35	0.340
0.64927E+15	0.48329E+35	0.370
0.70686E+15	0.62008E+35	0.400
0.76568E+15	0.77912E+35	0.430
0.82583E+15	0.96151E+35	0.460
0.88738E+15	0.11682E+36	0.490
0.95043E+15	0.13999E+36	0.520
0.10150E+16	0.16569E+36	0.550
0.10813E+16	0.19389E+36	0.580
0.11492E+16	0.22449E+36	0.610
0.12189E+16	0.25733E+36	0.640
0.12904E+16	0.29223E+36	0.670
0.13636E+16	0.32903E+36	0.700
0.14896E+16	0.39423E+36	0.750
0.16207E+16	0.46399E+36	0.800
0.17568E+16	0.53809E+36	0.850
0.18978E+16	0.61645E+36	0.900
0.20438E+16	0.69900E+36	0.950
0.21948E+16	0.78573E+36	1.000
0.25116E+16	0.97160E+36	1.100
0.28480E+16	0.11739E+37	1.200
0.32039E+16	0.13926E+37	1.300

symmetry energy ($E_{\rm sym} = 31$ MeV) but rather different symmetry energy slope L, it is clearly demonstrated that the radius sensitively depends on the symmetry energy slope with the maximum mass only slightly modified. It is the well accepted R versus L dependence mentioned in the introduction (e.g., Lattimer & Prakash 2004, 2001; Li & Steiner 2006). A smaller L (softer symmetry energy) leads to a smaller radius. The combined results for $\Lambda(1.4)$ are as shown in Figure 2. They all fulfill the GW170817 constraint of $\Lambda(1.4) \leqslant 800$ (Abbott et al. 2017). Different crust prescriptions could have influence on the resulting radius; we also test the crust dependence of tidal deformability by connecting the $L = 40$ MeV EOS model with four other crust models collected in our previous work (Li et al. 2016c). The resulting $\Lambda(1.4)$ is in the range of $324 \sim 344$, namely in the present study the crust influence of tidal deformability is limited to around 6 % for a $1.4\,M_\odot$ star.

We proceed to present in Figure 3 (Figure 4) the resulting Love numbers (tidal deformabilities) as a function of the mass and the compactness. The behaviors of k_2 and Λ follow the above analysis and are similar to previous calculations (e.g., Hinderer et al. 2010; Postnikov et al. 2010). In Figure 3, k_2 first increases then decreases with the mass and the compactness. In Figure 4, Λ monotonously decreases with the mass and the compactness. The increase of k_2 and large values of Λ for small masses (below $\sim 1.0\ M_\odot$) are due to large radii and large portions of soft crust matter. If no crust is considered (e.g., an EOS described by a pure polytropic function), k_2 will decrease monotonously with mass and compactness as well (Hinderer et al. 2010).

It is worthwhile to note that according to Figure 3, k_2 monotonically depends on L for all the mass range, i.e., for a star with a certain amount of mass (compactness), a larger L leads to a smaller k_2. However, as already seen in Figure 2 from $\Lambda(1.4)$, this monotonic dependence does not hold for Λ, since Λ is normalized with a factor of R^5. Hence, the differences in radius (according to the R versus L relation mentioned before) will scatter the dependence of Λ on L.

To better understand the relation between L and Λ, we present in Figure 5, for more L values, the results of both $\Lambda(1.4)$ and the mass-weighed tidal deformability ($\tilde{\Lambda}$). A chirp mass of $1.188\,M_\odot$ and mass ratio[3] of 0.7 are employed for the calculation of $\tilde{\Lambda}$ in a binary system. We can see that neither $\Lambda(1.4)$ nor $\tilde{\Lambda}$ shows correlation with L. In general, one expects large Λ at large L, since a large star (i.e., large R) tends to be easily deformed. However, Λ is anomalously large at small L (i.e., $L \leqslant 30$ MeV), which may be understood from the different smoothness behaviors in these cases at the crust-core matching interface, when core EOSs with different L are matched to the same inner crust EOS of Negele & Vautherin (1973). The importance of a matching interface has also been pointed out in our previous work (Li et al. 2016c) on the mass-equatorial radius relations of fast-spinning NSs, and deserves more study in the future. The violation of monotonic dependence of Λ on L is particularly interesting in terms of observations. As a consequence, a measurement of $\tilde{\Lambda}$ by GW observations does not necessarily translate into measurement of the radius of the NS, given the R versus L relation. A similar conclusion has also been recognized in the extended Skyrme-Hartree–Fock model (L. W. Chen et al. 2018, private communication).

In this section we provide the tabulated EOS in Table 3 for our best model (the case of $L = 40$ MeV), with satisfying descriptions of vacuum nucleon properties (r_N, m_N), nuclear matter properties (ρ_0, E/A, K, $E_{\rm sym}$, L, M_N^*), and astrophysical observations ($M_{\rm TOV}$, $\Lambda(1.4)$). We call this EOS the "QMF18" EOS. Without interpolation, the EOS data in Table 3 give $2.0805 M_\odot$ for $M_{\rm TOV}$, within an error of magnitude of $\sim 10^{-4}$: the complete data give $2.0809 M_\odot$.

We also collect other new NS EOSs from various many-body techniques. These EOSs, along with their mass–radius relations, are plotted in Figure 6. Their L and $M_{\rm TOV}$ values are also shown in Table 4, with $\tilde{\Lambda}$ and various results for a $1.4\,M_\odot$ star: $R(1.4)$, $M/R(1.4)$ and $\Lambda(1.4)$. The EOSs of NL3$\omega\rho$, DDME2, and DD2 are from the RMF model (Fortin et al. 2016). The EOSs of density-dependent relativistic Hartree-Fock (DDRHF) and DDRHFΔ are from the DDRHF theory, with the latter extended to include Δ-isobars (Zhu et al. 2016). The Sly9 EOS is from the Skyrme functional (Fortin et al. 2016). The Barcelona–Catania–Paris–Madrid (BCPM) EOS, named after the BCPM energy density functional (Sharma et al. 2015), is based on the microscopic Brueckner–Hartree–Fock theory (Baldo 1999).

[3] As pointed out by e.g., (Radice et al. 2018), the mass-weighted tidal deformability is expected to be very weakly dependent on the mass ratio. Hence, considering one mass ratio case should be representative enough for analysis.

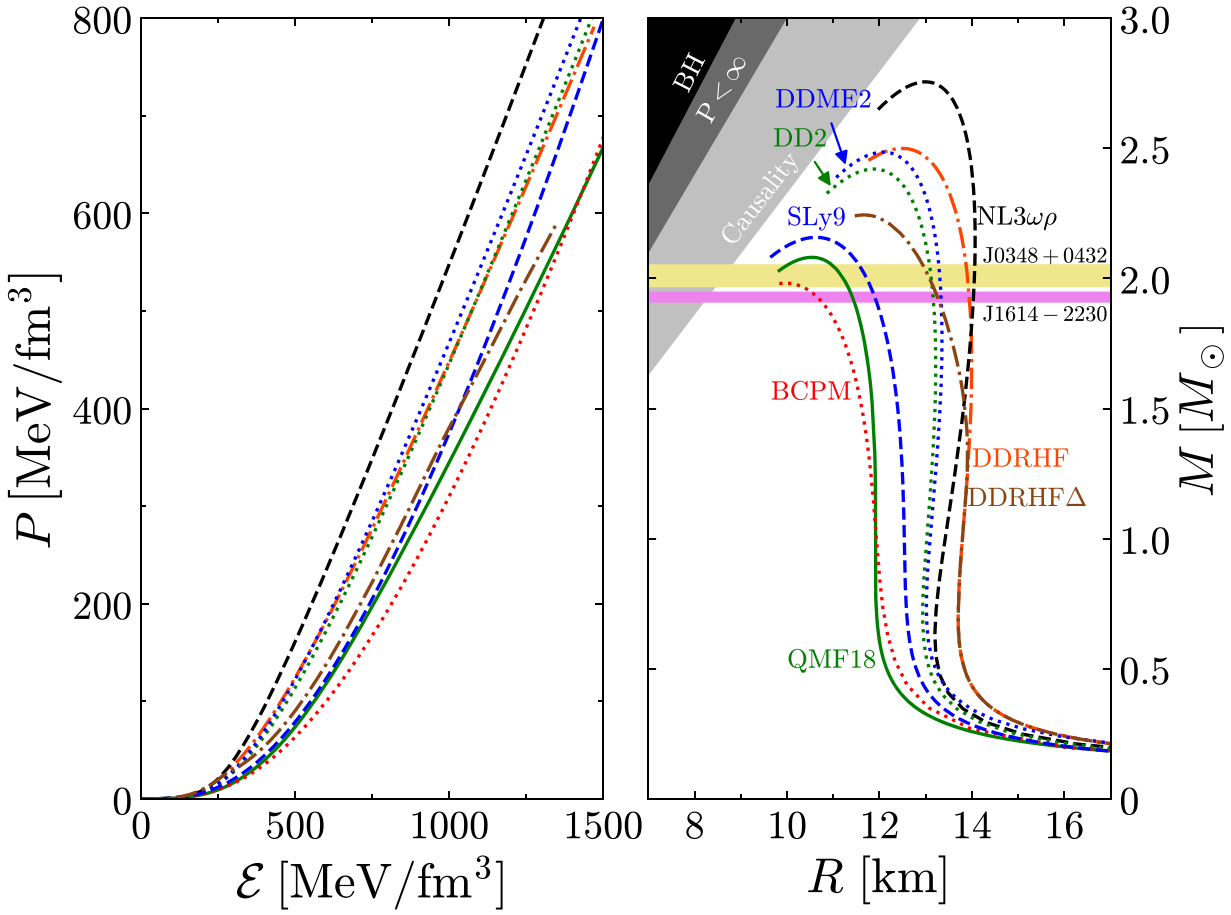

Figure 6. The new QMF18 EOS (left panel) and its mass relation (right panel), to be compared with the results of other recent NS EOSs from various many-body techniques: DDRHF, DDRHFΔ (Zhu et al. 2016), NL3$\omega\rho$, DDME2, DD2, Sly9 (Fortin et al. 2016), BCPM (Sharma et al. 2015). The mass measurements for two recent massive stars, PSR J1614-2230 (Demorest et al. 2010; Fonseca et al. 2016) and PSR J0348+0432 (Antoniadis et al. 2013), are also shown. The shaded regions show the black hole limit, the Buchdahl limit, and the causality limit, respectively.

Table 4
Radius, Compactness, and Tidal Deformability for a 1.4 $M_\odot$ Star, Provided for Various Advanced NS EOSs and Their Maximum Static Gravitational Mass $M_{\rm TOV}$ and Symmetry Energy Slope L

	QMF18	DDRHF	DDRHFΔ	NL3$\omega\rho$	DDME2	DD2	Sly9	BCPM
$M_{\rm TOV}$ ($M_\odot$)	2.08	2.50	2.24	2.75	2.48	2.42	2.16	1.98
L (MeV)	40	82.99	82.99	55.5	51.2	55.0	54.9	52.96
R(1.4) (km)	11.77	13.74	13.67	13.75	13.21	13.16	12.46	11.72
M/R(1.4)	0.1756	0.1505	0.1512	0.1503	0.1566	0.1571	0.1660	0.1765
Λ(1.4)	331	865	828	925	681	674	446	294
$\tilde{\Lambda}$	381.4–388.4	948.7–993.4	900.8–962.9	1002.9–1056.3	747.8–782.7	747.9–777.3	519.6–524.3	353.9–1056.3

Note. In the last line we have also shown the range of $\tilde{\Lambda}$ for a binary system with a chirp mass equal to 1.188 $M_\odot$ and mass ratio in the range of (0.7–1), which corresponds to the low-spin case for GW170817. This calculation shows the consistency between the constraint in $\tilde{\Lambda}$ and Λ(1.4). Furthermore, for the NL3$\omega\rho$ EOS, which possesses the largest value of Λ(1.4) among all the EOSs, $\tilde{\Lambda}$ can actually be as small as 712 if the mass ratio of the system is 0.4 (which corresponds to the 90 % credible range of the mass ratio in the high-spin assumption case for GW170817); hence, it is very close to the 90 % credible upper limit for $\tilde{\Lambda}$ in the high-spin case. Therefore, the possibility of this EOS would not be clearly excluded if the high-spin case is taken into account, as also seen in Nandi & Char (2018).

We see that the tidal deformability has a roughly positive relation to the symmetry energy slope L: a smaller L usually leads to a smaller Λ(1.4). Nevertheless, Λ(1.4) depends not only on the saturation properties (like L), but also on the high-density part of the EOS (imprinted onto $M_{\rm TOV}$). This is clearly seen in the comparison of the NL3$\omega\rho$ and DD2 cases, where, with the same $L \sim 55$ MeV, Λ(1.4) drops from 925 for NL3$\omega\rho$, to 674 for DD2, resulting from a much lowered $M_{\rm TOV}$ value in the DD2 case: 2.75 versus 2.42 $M_\odot$. We note that, besides NL3$\omega\rho$, the DDRHF results with a representative parameter set PKO3 are not consistent with the $\Lambda(1.4) \leqslant 800$ constraint of GW170817 for the low-spin prior, but are allowed by a more loosely constrained upper limit of 1400 for the high-spin prior (Abbott et al. 2017). Also, possible strangeness phase transitions (e.g., Δ-isobars Zhu et al. 2016), soften the high-density EOS and lower the maximum static gravitational mass $M_{\rm TOV}$, leading to relatively small values of Λ(1.4): 865 (for DDRHF) versus 828 (for DDRHFΔ).

4. Summary

In the era of gravitational wave astronomy, the unknown EOS of supranuclear matter could soon be understood thanks to accruing studies on gravity, astrophysics, and nuclear physics. The present work timely constructs a new EOS for NSs in the quark level, respecting all available constraints from terrestrial nuclear laboratory experiments and astrophysical observations, including the recent GW170817 constraint on the tidal deformability.

We employ the QMF model, where constituent quarks are confined by a harmonic oscillator confining potential. We first determine the quark potential parameter by reproducing the properties of the nucleon in free space. Corrections due to center-of-mass motion, quark-pion coupling, and one gluon exchange are included to obtain the nucleon mass. Then, the many-body nucleonic system is studied in the mean-field level, with the meson coupling constants newly fitted by reproducing the empirical saturation properties of nuclear matter, including the recent determinations of symmetry energy parameters. The predicted star properties can fulfill the recent two-solar-mass constraint and the 800 constraint for the dimensionless tidal deformability of a 1.4 $M_{\odot}$ star.

In particular, we explore the relation of the tidal deformability to an uncertain parameter of the symmetry energy slope at saturation. We discuss not only modifying the slope value in its empirical range in one model, but also comparing the results of various many-body techniques. We find no evidence for a simple relation between the symmetry energy slope (hence the radius) and tidal deformability (either $\Lambda(1.4)$ or $\tilde{\Lambda}$). Consequently, claims regarding constraining NS radius with tidal deformability measurements should be considered with caution.

In future works, considering this line of inquiry, we can perform detailed studies of tidal deformability on the interplay of the saturation parameters with various possible strangeness phase transitions at higher densities (usually above $2\rho_0$), e.g., hyperons, kaon condensation, and Δ-isobars (Li et al. 2006, 2007, 2010; Burgio et al. 2011; Hu et al. 2014b; Zhu et al. 2016). We can also extend the present study to a unified treatment of both the hadron phase and the quark phase, to better explore the quark deconfinement phase transition in dense matter and the properties of hybrid stars (e.g., Li et al. 2015). An extended QMF18 EOS with unified crust and core properties will be useful as well for supernova simulations or pulsar studies. Pulsar properties can be predicted (e.g., Li et al. 2016a) and updated studies can be performed for short gamma-ray bursts (e.g., Li et al. 2016b, 2017). An extension of the current QMF model, that includes a spherical bag for confinement, is in progress (Zhu et al. 2018).

We thank Bao-An Li and Antonios Tsokaros for valuable discussions. E.Z. is grateful to the China Scholarship Council for supporting the joint PhD training project. The work was supported by the National Natural Science Foundation of China (No. U1431107).

ORCID iDs

Ang Li https://orcid.org/0000-0001-9849-3656

References

Abbott, B. P., Abbott, R., Abbott, T. D., et al. 2017, PhRvL, 119, 161101
Ai, S., Gao, H., Dai, Z.-G., et al. 2018, ApJ, 860, 57
Annala, E., Ecker, C., Hoyos, C., et al. 2018, PhRvL, 120, 172703
Annala, E., Gorda, T., Kurkela, A., & Vuorinen, A. 2017, arXiv:1711.02644
Antoniadis, J., Freire, P. C. C., Wex, N., et al. 2013, Sci, 340, 448
Baldo, M. 1999, Nuclear Methods and the Nuclear Equation of State, Vol. 8 (Singapore: World Scientific)
Barik, N., & Dash, B. K. 1986, PhRvD, 33, 1925
Barik, N., Mishra, R. N., Mohanty, D. K., Panda, P. K., & Frederico, T. 2013, PhRvC, 88, 015206
Bauswein, A., Just, O., Janka, H.-T., & Stergioulas, N. 2017, ApJL, 850, L34
Baym, G., Pethick, C., & Sutherland, P. 1971, ApJ, 170, 299
Boguta, J., & Bodmer, A. R. 1977, NuPhA, 292, 413
Burgio, G. F., Schulze, H.-J., & Li, A. 2011, PhRvC, 83, 025804
Centelles, M., Roca-Maza, X., Viñas, X., & Warda, M. 2009, PhRvL, 102, 122502
Chodos, A., Jaffe, R. L., Johnson, K., Thorn, C. B., & Weisskopf, V. F. 1974, PhRvD, 9, 3471
Cozma, M. D., Leifels, Y., Trautmann, W., Li, Q., & Russotto, P. 2013, PhRvC, 88, 044912
Damour, T., & Nagar, A. 2009, PhRvD, 80, 084035
Damour, T., Soffel, M., & Xu, C. 1992, PhRvD, 45, 1017
Danielewicz, P., Lacey, R., & Lynch, W. G. 2002, Sci, 298, 1592
Danielewicz, P., & Lee, J. 2014, NuPhA, 922, 1
Demorest, P. B., Pennucci, T., Ransom, S. M., Roberts, M. S. E., & Hessels, J. W. T. 2010, Natur, 467, 1081
Drago, A., & Pagliara, G. 2018, ApJL, 852, L32
Fattoyev, F. J., Carvajal, J., Newton, W. G., & Li, B.-A. 2013, PhRvC, 87, 015806
Fattoyev, F. J., Piekarewicz, J., & Horowitz, C. J. 2018, PhRvL, 120, 172702
Fonseca, E., Pennucci, T. T., Ellis, J. A., et al. 2016, ApJ, 832, 167
Fortin, M., Providência, C., Raduta, A. R., et al. 2016, PhRvC, 94, 035804
Frederico, T., Carlson, B. V., Rego, R. A., & Hussein, M. S. 1989, JPhG, 15, 297
Guichon, P. A. M. 1988, PhLB, 200, 235
Hinderer, T. 2008, ApJ, 677, 1216
Hinderer, T., Lackey, B. D., Lang, R. N., & Read, J. S. 2010, PhRvD, 81, 123016
Horowitz, C. J., & Piekarewicz, J. 2001, PhRvL, 86, 5647
Hu, J. N., Li, A., Shen, H., & Toki, H. 2014a, PTEP, 2014, 013D02
Hu, J. N., Li, A., Toki, H., & Zuo, W. 2014b, PhRvC, 89, 025802
Krastev, P. G., & Li, B.-A. 2018, arXiv:1801.04620
Lattimer, J. M., & Prakash, M. 2001, ApJ, 550, 426
Lattimer, J. M., & Prakash, M. 2004, Sci, 304, 536
Li, A., Burgio, G. F., Lombardo, U., & Zuo, W. 2006, PhRvC, 74, 055801
Li, A., Dong, J. M., Wang, J. B., & Xu, R. X. 2016a, ApJS, 223, 16
Li, A., Zhang, B., Zhang, N.-B., et al. 2016b, PhRvD, 94, 083010
Li, A., Zhang, N. B., Qi, B., & Burgio, G. F. 2016c, arXiv:1610.08770
Li, A., Zhou, X. R., Burgio, G. F., & Schulze, H.-J. 2010, PhRvC, 81, 025806
Li, A., Zhu, Z.-Y., & Zhou, X. 2017, ApJ, 844, 41
Li, A., Zuo, W., Mi, A.-J., & G, B. 2007, ChPhy, 16, 1934
Li, A., Zuo, W., & Peng, G. X. 2015, PhRvC, 91, 035803
Li, B.-A., Chen, L.-W., & Ko, C. M. 2008, PhR, 464, 113
Li, B.-A., & Han, X. 2013, PhLB, 727, 276
Li, B.-A., & Steiner, A. W. 2006, PhLB, 642, 436
Li, D., & Pan, Z. 2016, RaSc, 51, 1060
Li, J. J., Long, W. H., & Sedrakian, A. 2018a, arXiv:1801.07084
Li, T., Xiong, S., Zhang, S., et al. 2018b, SCPMA, 61, 031011
Long, W. H., Sun, B. Y., Hagino, K., & Sagawa, H. 2012, PhRvC, 85, 025806
Ma, P.-X., Jiang, J.-L., Wang, H., et al. 2017, arXiv:1711.05565
Margalit, B., & Metzger, B. D. 2017, ApJL, 850, L19
Mishra, R. N., Sahoo, H. S., Panda, P. K., Barik, N., & Frederico, T. 2015, PhRvC, 92, 045203
Mishra, R. N., Sahoo, H. S., Panda, P. K., Barik, N., & Frederico, T. 2016, PhRvC, 94, 035805
Müller, H., & Serot, B. D. 1996, NuPhA, 606, 508
Nandi, R., & Char, P. 2018, ApJ, 857, 12
Negele, J. W., & Vautherin, D. 1973, NuPhA, 207, 298
Özel, F., Psaltis, D., Arzoumanian, Z., Morsink, S., & Bauböck, M. 2016, ApJ, 832, 92
Paschalidis, V., Yagi, K., Alvarez-Castillo, D., Blaschke, D. B., & Sedrakian, A. 2018, PhRvD, 97, 084038
Piekarewicz, J. 2010, JPhG, 37, 064038
Postnikov, S., Prakash, M., & Lattimer, J. M. 2010, PhRvD, 82, 024016
Radice, D., Perego, A., Zappa, F., & Bernuzzi, S. 2018, ApJL, 852, L29
Ray, P. S., Chakrabarty, D., Wilson-Hodge, C. A., et al. 2010, Proc. SPIE, 7732, 773248
Ruiz, M., Shapiro, S. L., & Tsokaros, A. 2018, PhRvD, 97, 021501

Saito, K., Tsushima, K., & Thomas, A. W. 2007, PrPNP, 58, 1
Serot, B. D., & Walecka, J. D. 1986, AdNuP, 16, 1
Sharma, B. K., Centelles, M., Viñas, X., Baldo, M., & Burgio, G. F. 2015, A&A, 584, A103
Shen, H., & Toki, H. 2000, PhRvC, 61, 045205
Shen, H., & Toki, H. 2002, NuPhA, 707, 469
Shibata, M., Fujibayashi, S., Hotokezaka, K., et al. 2017, PhRvD, 96, 123012
Shlomo, S., Kolomietz, V. M., & Colò, G. 2006, EPJA, 30, 23
Sun, B. Y., Long, W. H., Meng, J., & Lombardo, U. 2008, PhRvC, 78, 065805
Toki, H., Meyer, U., Faessler, A., & Brockmann, R. 1998, PhRvC, 58, 3749
Tsang, M. B., Zhang, Y., Danielewicz, P., et al. 2009, PhRvL, 102, 122701
Walecka, J. D. 1974, AnPhy, 83, 491
Watts, A., Espinoza, C. M., Xu, R., et al. 2015, in Advancing Astrophysics with the Square Kilometre Array (AASKA14) (Trieste: SISSA), 43
Watts, A., Yu, W., Poutanen, J., et al. 2018, SCPMA, in press
Xing, X., Hu, J., & Shen, H. 2016, PhRvC, 94, 044308
Zhang, N.-B., Li, B.-A., & Xu, J. 2018, arXiv:1801.06855
Zhang, Z., & Chen, L.-W. 2015, PhRvC, 92, 031301
Zhou, E., Zhou, X., & Li, A. 2018, PhRvD, 97, 083015
Zhu, Z.-Y., & Li, A. 2018, PhRvC, 97, 035805
Zhu, Z.-Y., Li, A., Hu, J., & Shen, H. 2018, arXiv:1805.04678
Zhu, Z.-Y., Li, A., Hu, J.-N., & Sagawa, H. 2016, PhRvC, 94, 045803